# Kent Academic Repository

Zhu, Xiaoyu, Xu, Chuanlong, Hossain, MD Moinul, Liu, Yan and Cheong Khoo, Boo (2024) *Accurate weight coefficient estimation of multi-camera light field PIV through backpropagation neural network.* Measurement, 226 . ISSN 0263-2241.

# Accurate weight coefficient estimation of multi-camera light field PIV through backpropagation neural network

**Abstract:** Volumetric velocity measurement through multi-camera light field particle image velocimetry (LF-PIV) requires an accurate estimation of the weight coefficient (WC) of three-dimensional (3D) tracer particle distribution reconstruction. To achieve that, this study proposes a calibration method based on a backpropagation neural network (BP-NN) for the WC estimation of the multi-camera LF-PIV. The BP-NN model establishes a mapping relationship between the spatial voxels and pixels of the multi-cameras. The proposed method is compared with the direct ray tracing (DRT) method and it shows that the proposed method provides an accurate estimation of the WC. It also does not depend on the prior knowledge of angle separations of the multi-cameras as is required for the DRT method. The proposed method is initially evaluated by conducting synthetic tests of ring vortex field reconstruction and further verified by conducting experiments on a low-swirl injector (LSI) flow. Results show that the root mean square error of the ring vortex displacement field can be reduced from 0.71 voxels to 0.35 voxels by the proposed method. The relative errors of LSI flow axial and radial velocity components are smaller than 10%. Therefore, it demonstrates that the 3D flow velocity can be measured accurately by the multi-camera LF-PIV by incorporating the proposed BP-NN calibration method.

**Keywords:** Light field PIV; Multiple cameras; Calibration; Weight coefficient estimation; Backpropagation neural network

# 1. Introduction

Recovering the complete topology of unsteady flow structures is challenging and it has great interest in fluid mechanic studies [1]. Due to the intrinsically three-dimensional (3D) nature of the unsteady flows, it is desirable to depict the full flow field within a measurement volume. To achieve that, continuous efforts have been devoted to developing advanced volumetric velocimetry techniques [2] such as the multi-camera-based tomographic PIV (Tomo-PIV) and defocusing PIV (DPIV), single-camera-based scanning PIV (SPIV) and light field PIV (LF-PIV). Among these techniques, the LF-PIV allows instantaneous 3D flow field measurement via a single camera and shows a compelling prospect for applications where optical windows are limited [3-5]. However, a lower accuracy of velocity measurement can be observed along the optical axis direction due to the limited viewing aperture of the single camera [6,7]. To overcome this drawback, the effective approach is to add extra LF cameras (i.e., multi-camera LF-PIV) to capture the flow field information from different perspectives and thus improve the accuracy of the 3D flow measurement [8-10].

In the multi-camera LF-PIV, the 3D tracer particle distribution can be reconstructed from the LF images captured from different viewpoints for flow velocity estimation [11,12]. This is typically an inverse problem and can be resolved by the algebraic reconstruction technique, which requires an accurate estimation of the weight coefficient (WC) (i.e., the intensity contributions of the spatial voxels to the image pixels). Theoretically, the WC can be estimated using the direct ray-tracing (DRT) technique based on a thin lens model [13,14]. However, the thin lens model fails to account for ray deflections arising from real-world optical distortions (caused by the optical misalignment, lens nonlinearity and refractive index changes [15]) and affects the WC estimation, thus degrading the particle reconstruction and velocity measurement accuracy.

Several models have been developed to correct the optical distortions of the single camera-based imaging system. For instance, Soloff et al. [16] presented a calibration method for the planar PIV system by integrating several mapping functions to correct the optical distortions. Bok et al. [17] and Sun et al. [18] proposed a geometric calibration method for the unfocused and focused LF cameras, respectively, to correct the optical distortions and obtain the intrinsic and extrinsic of the LF cameras. Shi et al. [19] developed a volume calibration technique for the single-camera LF-PIV. A relationship between the object and image points is established based on the linear optics and various calibration parameters are used to correct the optical distortions. Hall et al. [20] proposed a direct LF calibration method for the LF-PIV and particle tracking velocimetry (PTV). A polynomial mapping function is employed by creating 4D LF coordinates to correct the lens distortions. These methods effectively correct the ray deflections caused by the lens distortion for the single-camera LF-PIV [21,22], however, the multi-camera calibration is challenging as it needs a repetitive process for each camera. More importantly, the single-camera calibration process does not account for the spatial information of the multiple cameras (e.g., angle separations and distances), which hinders the alignment of the particle volume reconstruction from different viewpoints. As a result, it creates reconstruction artefacts like ghost particles and elongation effect. To resolve this issue, an advanced calibration method for multi-camera systems is required to ensure that multiple cameras reconstruct the same particle volume [23]. Instead of recovering the particle volume from each viewpoint individually and combining the different particle volumes, a mapping that relates different cameras to a common-world coordinate system can be established via the calibration process. Through this

mapping relationship, a single particle volume can be reconstructed from images captured by multiple cameras.

In the conventional imaging-based tomographic PIV (i.e., without the MLA), the multi-camera calibration can be conducted by a volume self-calibration technique [24]. This technique leverages the triangulation method to compute the tracer particle positions and utilizes the residual triangulation error (referred to as disparity) to correct the mapping functions for all cameras [25]. However, this technique cannot directly be utilized for the multi-camera LF-PIV since the triangulation method requires focused images of the tracer particles, which are difficult to obtain in the LF imaging due to the absence of the MLA in front of the photosensor. In LF imaging, as the object scene is imaged by the main lens and microlens array (MLA) [26], respectively, the mapping that relates the object points to different LF cameras can be created in two steps, such as (*i*) the spatial voxels and the microlens on different LF cameras can be correlated by incorporating the propagation direction information of the light rays and (*ii*) the light rays can be extended from the MLA to the photosensor to link the spatial voxels with the image pixels. Through the established mapping, the WC of the voxels for different LF cameras can then be calculated.

To create the mapping between the voxels and pixels, polynomial models can be employed [27,28]. The accuracy of the polynomial model relies on the order of the polynomial. Results show that a third-order polynomial model can provide accurate calibration for the single-camera system [20]. However, the order and the complexity of the polynomial model increase rapidly with the number of cameras. As an alternative, the artificial neural network (ANN) can be used for high-order nonlinear fitting tasks [29,30]. Unlike the polynomial model that gives an explicit mathematical mapping, the ANN provide an implicit mapping between the input and output. Leveraging the generalized high-order fitting capacity and flexible network architecture, ANN has been used for the calibration of the stereoscopic systems for 3D positioning [31] and PTV [32].

Therefore, it is evident based on the state-of-the-art that an accurate estimation of the WC is essential to reconstruct the particle distribution and hence to measure the 3D flow velocity through the multi-camera LF-PIV. A calibration method is proposed for an accurate WC estimation of the multi-camera LF-PIV system. The calibration method is based on a backpropagation neural network (BP-NN), which is initially employed for mapping the spatial voxels to the microlens of the different LF cameras and then utilized to relate the voxels to the image pixels for the WC estimation. Compared to the current DRT method, the proposed method does not require the angle separations of multiple cameras as prior knowledge and is easy to implement in practical applications. Synthetic tests of 3D vortex field reconstructions are performed to verify the proposed method and experimental measurements on a low-swirl injector flow are further conducted to evaluate its performance. A detailed description of the proposed method is given and results derived from the synthetic and experimental tests are presented and discussed.

## 2. Principle of Multi-camera LF-PIV

### 2.1 Imaging model

The principle of the multi-camera LF-PIV is illustrated in Fig. 1. The tracer particles are immersed in the test flow field and a high-energy dual-pulse laser is used to provide illumination. The tracer particle motions are recorded by the multiple LF cameras (two in this study) from different perspectives. The LF images of the particles are initially pre-processed to eliminate the background noise and the simultaneous multiplicative algebraic reconstruction technique (SMART)

[33] is then used to reconstruct the particle volumes. The WC of the SMART is calculated through the BP-NN-based calibration procedure. Each pair of reconstructed particle volumes is then fed into the cross-correlation (CC) algorithm to estimate the 3D velocity field of the test flow.
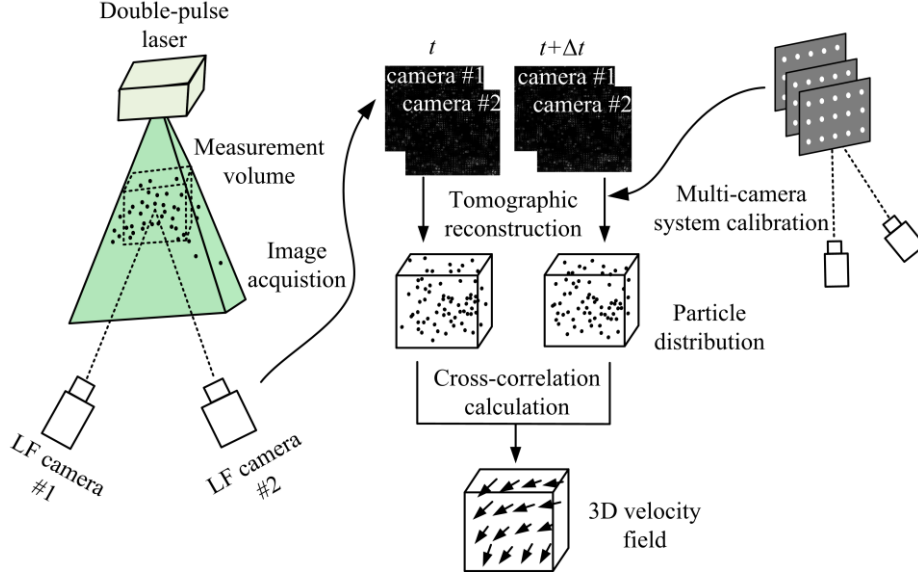


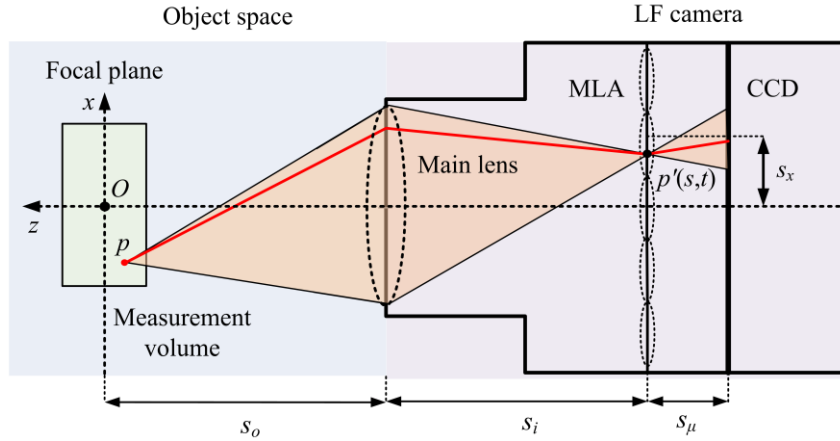Fig. 1 Principle of LF-PIV utilizing multiple LF cameras.



Fig. 2 Light ray propagation of the LF imaging based on geometrical optics.

Considering that the diffraction of the macroscopic imaging system is not significant, geometrical optics is a good approximation model for analyzing the actual behavior of light ray propagation. Where the light can be discretized as a large number of rays in different propagation directions (as illustrated in Fig. 2) and the propagation trajectories of the rays can be described by the ray transfer matrix [13]. In the multi-camera system, the world and camera coordinates may not be aligned perfectly and hence angle separation may exist. Therefore, the transformation of light rays between the world and camera coordinates is required to be performed accurately. For example, considering the LF camera #2 illustrated in Fig. 3, the world coordinates $(x, y, z)$ can be converted to the camera coordinates $(x_c, y_c, z_c)$ based on the relationship of the spatial geometry, as

$$x_c = (x - z \cdot \tan \alpha) \cdot \cos \alpha \qquad (1)$$

$$y_c = y \qquad (2)$$

$$z_c = \frac{z}{\cos\alpha} + (x - z \cdot \tan\alpha) \cdot \sin\alpha \qquad (3)$$

where $\alpha$ is the angle separation between the world and camera coordinates. If the multi-camera system contains $N_c$ cameras, the coordinate transformations should be performed $N_c$ times with the known angles separation ($\alpha_1, \alpha_2, \ldots, \alpha_{Nc}$). The obtained camera coordinates are then fed into the ray transfer matrix to perform the ray tracing process and form the images of different LF cameras.
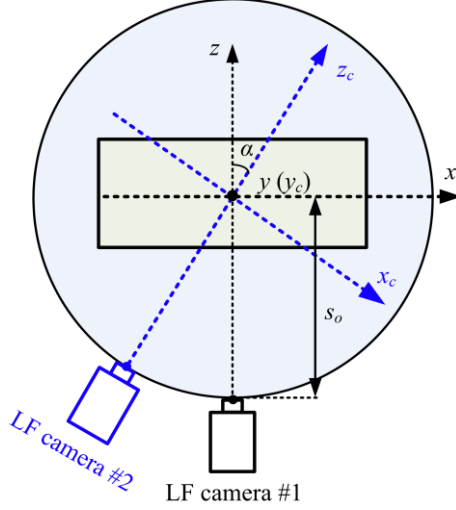


Fig. 3 Illustration of coordinate's transformation between the world and camera coordinates.

## 2.2 Particle volume reconstruction

The reconstruction of 3D particle distribution through multi-camera LF-PIV involves an inverse problem that is required to be solved. This can be formulated as a set of linear equations given as

$$w_{1,1,1} \cdot E_1 + w_{2,1,1} \cdot E_2 + \cdots + w_{j,1,1} \cdot E_j + \cdots + w_{M,1,1} \cdot E_M = I_{1,1}$$
$$\vdots$$
$$w_{1,i,1} \cdot E_1 + w_{2,i,1} \cdot E_2 + \cdots + w_{j,i,1} \cdot E_j + \cdots + w_{M,2,1} \cdot E_M = I_{i,1}$$
$$\vdots$$
$$w_{1,N,1} \cdot E_1 + w_{2,N,1} \cdot E_2 + \cdots + w_{j,i,1} \cdot E_j + \cdots + w_{M,N,1} \cdot E_M = I_{N,1}$$
$$\vdots$$
$$w_{1,1,q} \cdot E_1 + w_{2,1,q} \cdot E_2 + \cdots + w_{j,1,q} \cdot E_j + \cdots + w_{M,1,q} \cdot E_M = I_{1,q}$$
$$\vdots$$
$$w_{1,i,q} \cdot E_1 + w_{2,i,q} \cdot E_2 + \cdots + w_{j,i,q} \cdot E_j + \cdots + w_{M,2,q} \cdot E_M = I_{i,q}$$
$$\vdots$$
$$w_{1,N,q} \cdot E_1 + w_{2,N,q} \cdot E_2 + \cdots + w_{j,i,q} \cdot E_j + \cdots + w_{M,N,q} \cdot E_M = I_{N,q}$$
$$\vdots$$
$$w_{1,1,N_c} \cdot E_1 + w_{2,1,N_c} \cdot E_2 + \cdots + w_{j,1,N_c} \cdot E_j + \cdots + w_{M,1,N_c} \cdot E_M = I_{1,N_c}$$
$$\vdots$$
$$w_{1,i,N_c} \cdot E_1 + w_{2,i,N_c} \cdot E_2 + \cdots + w_{j,i,N_c} \cdot E_j + \cdots + w_{M,2,N_c} \cdot E_M = I_{i,N_c}$$
$$\vdots$$
$$w_{1,N,N_c} \cdot E_1 + w_{2,N,N_c} \cdot E_2 + \cdots + w_{j,i,N_c} \cdot E_j + \cdots + w_{M,N,N_c} \cdot E_M = I_{N,N_c} \qquad (4)$$

5

where $E_j$ denotes the intensity of $j_{th}$ voxel in the measurement volume ($j = 1\sim M$, $M$ is the total voxel number), $I_{i,q}$ denotes the intensity of $i_{th}$ pixel on the $q_{th}$ camera ($i = 1\sim N$, $N$ is the pixel number on the photosensor, $q = 1\sim N_c$), and $w_{j,i,q}$ denotes the WC of the $j_{th}$ voxel to the $i_{th}$ pixel. The order of the weight matrix (i.e., collection of all the voxels' WC) is usually smaller than the number of unknown voxels. Therefore the linear Eq. (4) is underdetermined and has a non-unique solution. To solve this equation, the SMART is used in terms of high computational efficiency. The iteration of the SMART is as follows

$$E_j^{k+1} = E_j^k \prod_i^{N_i} \left[ \left( \frac{I_i}{\sum_{m=1}^M w_{m,i} E_m^k} \right)^{\mu w_{j,i}} \right]^{1/N_i} \tag{5}$$

where $k$ denotes the $k_{th}$ iteration, $N_i$ is the number of pixels whose intensity is contributed by the $j_{th}$ voxel (referred to as affected pixels), and $\mu$ is the relaxation parameter.

To estimate the WC accurately for particle reconstruction, it is crucial to create a mapping relationship between the spatial voxels and the image pixels of different LF cameras. In contrast to the traditional CCD/CMOS camera with a single lens and a photosensor, the LF camera has a dense MLA and the object scene is imaged by the main lens and MLA, respectively during the LF imaging process. Thus, the calibrations are conducted in two steps for the multiple LF cameras. Initially, the BP-NN is established to relate the spatial voxels (which can be discretized as many object points) to the microlens of different LF cameras. Subsequently, the light rays are extended from the microlens to the photosensor to link the spatial voxels with the image pixels.

## 3. Calibration of multi-camera LF-PIV

### 3.1 Neural network-based calibration

*(1) Architecture of BP-NN*

The BP-NN is a multi-layer feedforward neural network that leverages the forward propagation error to tune the weights of the network. The architecture of the BP-NN is illustrated in Fig. 4. It is used to relate the object point location (e.g., point $p$ in Fig. 2) to the microlens position (e.g., point $p'$ in Fig. 2) by incorporating the propagation direction information of the light rays. The network consists of the inputs, hidden and output layers and outputs. The inputs are the world coordinate of the object point ($x$, $y$, $z$) and the main aperture positions that the ray passes through ($u_1$, $v_1$, $u_2$, $v_2$,···, $u_{Nc}$, $v_{Nc}$). The outputs are the positions that the ray hits on the microlenses ($s_1$, $t_1$, $s_2$, $t_2$, ···, $s_{Nc}$, $t_{Nc}$). The hidden layer of the network is defined as

$$P = \sigma \left[ W_h \left( x, y, z, u_1, v_1, u_2, v_2, \cdots u_q, v_q, \cdots u_{N_c}, v_{N_c} \right) + b_h \right] \tag{6}$$

where $W_h$ and $b_h$ denote the weight and bias of the hidden layer, respectively, and $P$ is the output of the hidden layer and is transformed by the sigmoid functions and inserted into the output layer. The structure of the output layer is similar to the hidden layer, defined as

$$Q = PW_o + b_o \tag{7}$$

where $W_o$ is the weight of the output layer and $b_o$ is the bias. The outcome of the output layer $Q$ is transformed by the linear transfer function and the final output is then attained.
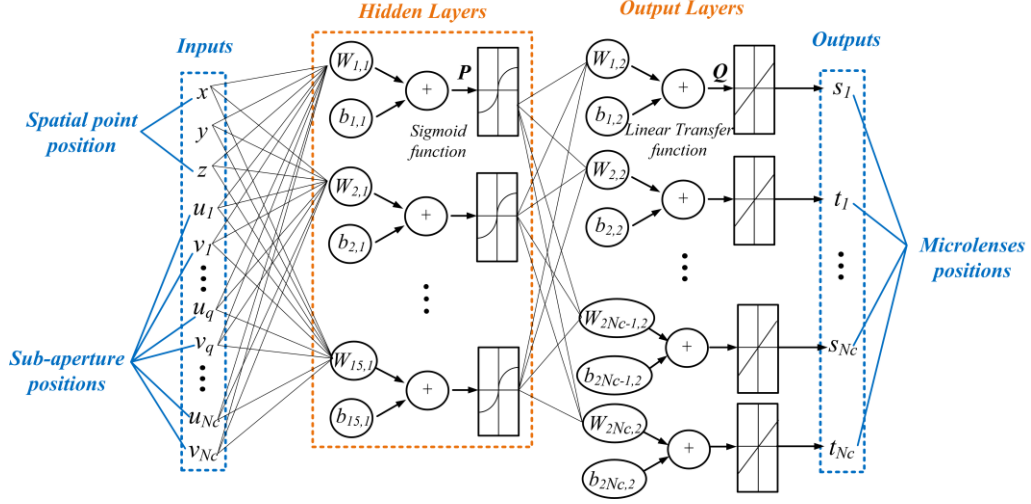
Fig.4 Architecture of the BP-NN model.

*(2) Generation of the dataset*

To train the BP-NN for accurate prediction of microlens positions, a calibration board that contains a dot point array is employed to generate the training dataset. The calibration board is moved to span the entire measurement volume, forming a 3D cloud of feature points with known world coordinates. Multiple LF cameras are employed to record the LF images of the dot board at different depths. The sub-aperture images of the dot points are subsequently extracted from the raw images for determining the main aperture and microlens positions that the rays pass through [i.e., $(u, v)$ and $(s, t)$ in Fig. 4].
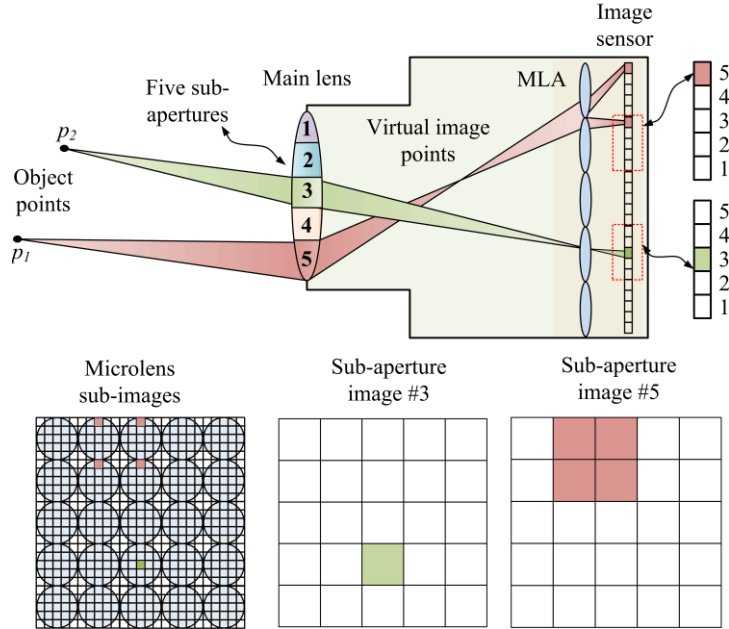


Fig.5 Extraction of the LF sub-aperture images.

The extraction of the sub-aperture images from a LF raw image is illustrated in Fig. 5. Since the separation between the MLA and the photosensor is equal to the focal length of the MLA, the

main lens and photosensor are approximately conjugated. In this case, the rays that hit the same pixel behind each microlens must originate from a specific sub-aperture of the main lens (e.g., the rays that reach pixels #3 and #5 are from sub-apertures #3 and #5, respectively). By extracting the corresponding pixel behind each microlens, the projections of the object point under a specific sub-aperture $(u, v)$ can be acquired. Figure 6 shows an example of the LF raw image of the dot board and the extracted sub-aperture image. The dot centers of the sub-aperture image are identified by the Gaussian fitting method [34]. The image coordinate of the dot center $(s_p, t_p)$ is transformed to the physical coordinate $(s, t)$ according to the microlens pitch $(p_m)$, and the microlens position that the ray passes through is therefore determined.



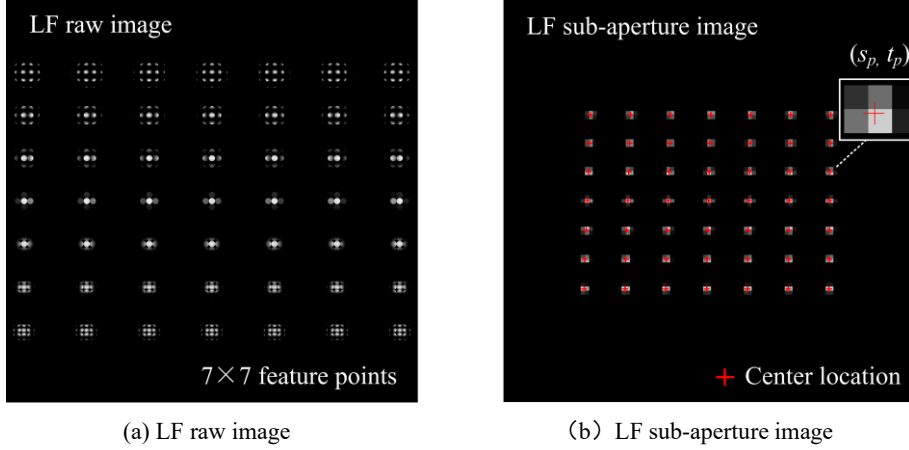(a) LF raw image            （b）LF sub-aperture image

Fig. 6 LF raw image and sub-aperture image of a dot calibration board.

For the multi-camera LF-PIV, the extraction of the sub-aperture image and identification of the dot center are conducted individually for each camera to construct the training dataset. If the number of feature points on the calibration board is $n_f$, the number of sub-aperture images extracted from a single LF raw image is $n_p$, and the calibration board is captured at $n_d$ different depths, a total of $n_f \times n_d \times n_p$ sets of input and output data can be obtained. For the BP-NN model, the complete dataset is divided into training, validating and testing at a ratio of 70%, 15% and 15%, respectively. The testing dataset is used to assess the accuracy and generalization of the model.

*(3) Parameters selection*

To ensure the prediction accuracy of the BP-NN, the training method and the number of hidden layers are required to be well chosen. In this study, training methods such as the Levenberg-Marquardt method (LM), Bayesian regularization method (BR) and gradient descent with momentum method (GDM) are compared under different numbers of the hidden layer ($N_l = 5$, 10, 15, 20 and 25). The node in each hidden layer is empirically optimized as 10. The accuracy of the BP-NN is evaluated by calculating the position prediction error normalized by the pitch of microlens ($p_m$), defined as

$$\sigma_{nor} = \frac{\sum_{i=1}^{N_t} \sqrt{\left(s_{tr} - s_{pr}\right)^2 + \left(t_{tr} - t_{pr}\right)^2}}{N_t \cdot p_m} \tag{8}$$

where $\sigma_{nor}$ is the normalized prediction error, $(s_{tr}, t_{tr})$ and $(s_{pr}, t_{pr})$ are the true and predicted microlens positions, respectively. $N_t$ is the number of test data.

Table 1 summarizes the normalized prediction error of the BP-NN model for a dual-camera system ($n = 2$). It can be observed that the $\sigma_{nor}$ of the GDM method is always higher under different $N_l$, while the error of the LM and BR methods is much lower. The $\sigma_{nor}$ of the LM and BR methods is about 0.04 microlens pitch when $N_l$ exceeds 10. The LM algorithm, which offers a faster training process compared to the BR method is selected to train the BP-NN model. To ensure high prediction accuracy and prevent overfitting, 15 hidden layers are incorporated in the BP-NN.

Table 1: Normalized prediction error ($\sigma_{nor}$) of BP-NN using different training methods and hidden layers

| $N_l$ | LM | | BR | | GDM | |
|---|---|---|---|---|---|---|
| | LF camera #1 | LF camera #2 | LF camera #1 | LF camera #2 | LF camera #1 | LF camera #2 |
| 5 | 0.292 | 0.333 | 0.336 | 0.285 | 0.399 | 0.455 |
| 10 | 0.043 | 0.041 | 0.040 | 0.041 | 0.109 | 0.111 |
| 15 | 0.038 | 0.040 | 0.039 | 0.040 | 0.062 | 0.065 |
| 20 | 0.038 | 0.039 | 0.039 | 0.040 | 0.066 | 0.061 |
| 25 | 0.048 | 0.049 | 0.048 | 0.049 | 0.067 | 0.070 |
| 30 | 0.063 | 0.065 | 0.066 | 0.066 | 0.090 | 0.091 |

## 3.2 Weight coefficient calculation

With the microlens position ($s$, $t$) predicted by the BP-NN, the rays from the main aperture ($u$, $v$) are further traced to the photosensor to correlate the spatial point to the image pixels. This is achieved by using the ray transfer matrix, given as

$$\begin{pmatrix} x' \\ y' \\ \theta' \\ \phi' \end{pmatrix} = \begin{bmatrix} 1 & 0 & s_\mu & 0 \\ 0 & 1 & 0 & s_\mu \\ 0 & 0 & 1 & 0 \\ 0 & 0 & 0 & 1 \end{bmatrix} \left( \begin{bmatrix} 1 & 0 & 0 & 0 \\ 0 & 1 & 0 & 0 \\ -1/f_m & 0 & 1 & 0 \\ 0 & -1/f_m & 0 & 1 \end{bmatrix} + \begin{pmatrix} 0 \\ 0 \\ s_x/f_m \\ s_y/f_m \end{pmatrix} \right) \begin{pmatrix} s \\ t \\ (u-s)/s_i \\ (v-t)/s_i \end{pmatrix} \tag{9}$$

where $f_m$ denotes the focal length of the microlens, $s_u$ is the separation between the MLA and the photosensor, $s_x$ and $s_y$ are the distances from the microlens center to the optical axis.

To calculate the WC, point sources at different spatial positions are sampled within the voxel, and a large number of rays in different propagation directions are sampled from each point source. The BP-NN model and the ray transfer matrix described in Eq. (9) are utilized to determine the image pixels whose intensity is contributed by a particular voxel. The WC of the $j_{th}$ voxel to the $i_{th}$ pixel of the $q_{th}$ camera can then be calculated as

$$w_{j,i,q} = \frac{n_{j,i,q}}{n_{j,t}} \tag{10}$$

where $n_{j,t}$ denotes the total number of rays sampled from the $j_{th}$ voxel, and $n_{j,i,q}$ denotes the number of rays that enter the $i_{th}$ pixel of the $q_{th}$ camera. To calculate the accurate WC with high computational efficiency, the sampling number of the point sources within each voxel is set as 500 and the angle separation of the sampling light rays from each point source is set to 0.05°. Once the WC of all the discrete voxels is calculated, the reconstruction of particle distribution is performed by the SMART [Eq. (5)]. The overview of the calibration procedure of multi-camera LF-PIV based on the BP-NN model, as well as the reconstruction of tracer particles, is shown in Fig. 7.
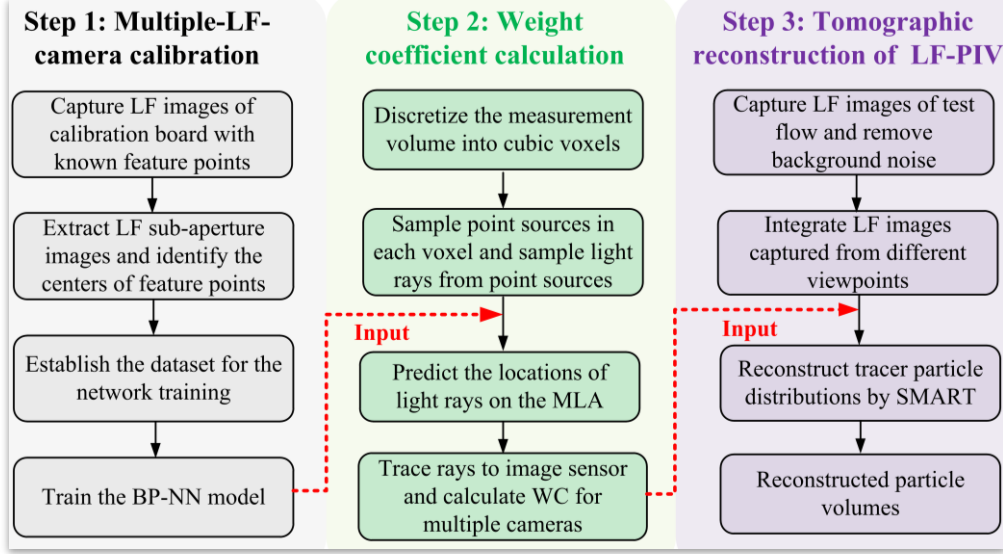
Fig 7 Overview of the calibration of multi-camera LF-PIV.

# 4. Numerical verification

To evaluate the accuracy of the proposed method, synthetic tests were carried out to reconstruct the random particle distributions and Gaussian vortex displacement field. In this study, a dual LF camera system is used to verify the proposed BP-NN calibration method through these synthetic tests. The dual LF-camera system is considered in terms of practical applicability such as the complexity of the system setup and the required optical access. Figure 8 illustrates the position of the measurement volume relative to the LF cameras and the defined world coordinate. The center of the measurement volume (i.e., origin) is aligned with the focal points of the two cameras. The separation angles of the cameras concerning the depth direction of the measurement volume ($\alpha_1$ and $\alpha_2$) are set to 45°.
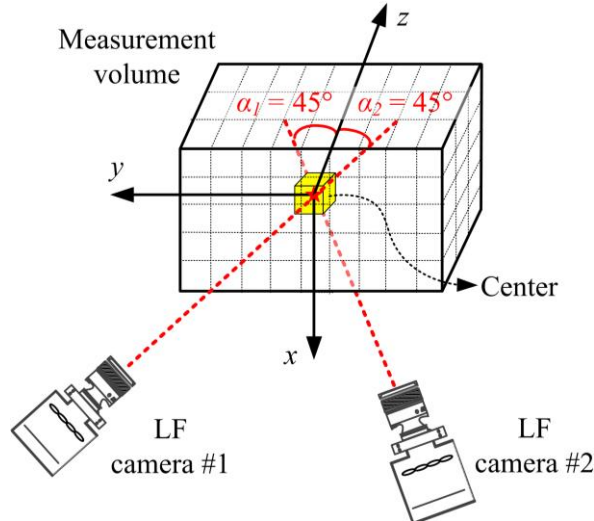


Fig. 8 Illustration of the measurement volume position relative to the dual-camera LF-PIV system.

Table 2: Optical parameters of the LF camera and conventional camera

| Parameter | LF camera | | Conventional camera (Used in Planar PIV) |
| --- | --- | --- | --- |
| | Simulation | Experiment | |
| Magnification of the main lens | -1 | -1 | -0.33 |
| Focal length of main lens | 100 mm | 100 mm | 100 mm |
| *f*-number of main lens | 4 | 4 | 2.8 |
| Focal length of microlens | 0.8 mm | 0.8 mm | - |
| *f*-number of microlens | 8 | 8 | - |
| Microlens pitch | 0.1 mm | 0.1 mm | - |
| Number of microlenses | 254×254 | 254×254 | - |
| Pixel size | 5.5 μm | 4.54 um | 4.45 μm |
| Number of pixels | 4000×4000 | 2208×2752 | 2208×2752 |
| Number of cameras | 2 | 2 | 1 |



(a) LF image of camera #1　　　　(b) LF image of camera #2
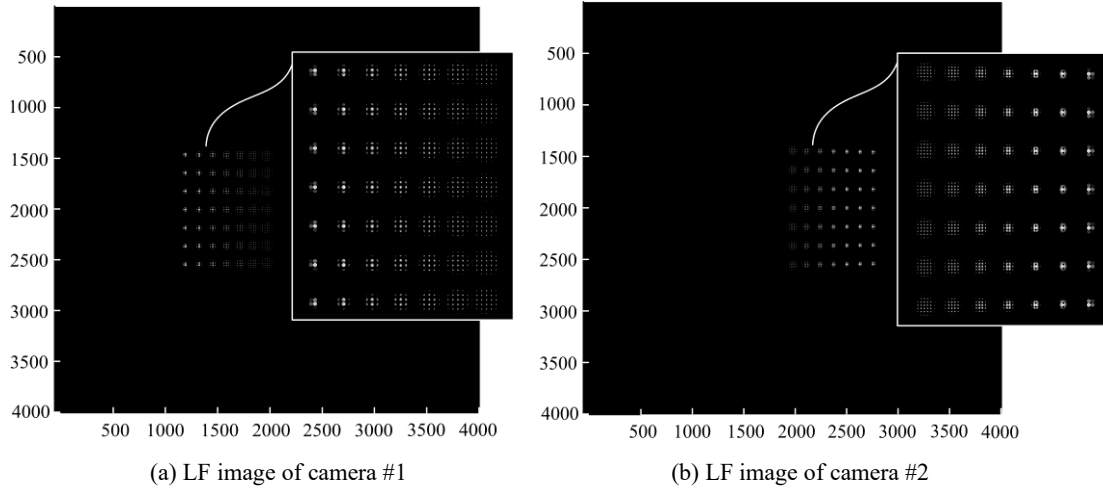
Fig. 9 Synthetic LF images of a virtual dot calibration board located at the depth of $z$ = -3 mm.

To investigate the calibration accuracy of the dual-LF camera system, a virtual calibration board composed of 7×7 dot points is generated. The calibration board is moved within the depth range of -10 mm < $z$ < 10 mm with a uniform interval of 1 mm. The spacing between each two dots is 1 mm and the dot diameter is 0.1 mm. Based on the LF imaging model described in Section 2, the synthetic LF images of the dot board at different locations are obtained. The optical parameters used to generate the synthetic LF images are summarized in Table 2. Figure 9 illustrates an example of the LF images captured by the two LF cameras. The WC is computed through the BP-NN calibration method as described in Section 3 and the SMART is used to reconstruct the particle volumes (10 iterations, $\mu$ = 1.0). For a comparative study, the DRT method is employed for the WC calculation. The DRT method traces the trajectories of the rays from the spatial points to the image sensor and calculates the WC by counting the number of rays received by a specific pixel [13]. The DRT requires prior knowledge of the angle separation of the cameras based on the measurement volume (i.e., $\alpha_1$ and $\alpha_2$ in Fig. 8), in practice, it is difficult to measure precisely. Therefore, an error term of the angle separation of the cameras is involved in the DRT, as

$$\alpha_{1m} = \alpha_1 + \Delta\alpha \tag{11}$$

$$\alpha_{2m} = \alpha_2 + \Delta\alpha \tag{12}$$

where $\alpha_1$, $\alpha_2$ and $\alpha_{1m}$, $\alpha_{2m}$ are the true and measured angle separation, respectively, and $\Delta\alpha$ is the error term in terms of angle separation. In the synthetic test of the particle distribution reconstruction, $\Delta\alpha$ is set as 0° (i.e., no error in the angle separation of the camera) and the reconstruction quality of the DRT-SMART and BP-NN-SMART is compared. For the ring vortex reconstruction, $\Delta\alpha$ is set as $\Delta\alpha = 0°$ and $\Delta\alpha = 1°$, respectively, and the reconstruction accuracy of the 3D displacement fields achieved by the DRT-SMART and BP-NN-SMART is compared.

## 4.1 Particle distribution reconstruction

For the particle distribution reconstruction, synthetic particle fields with known particle distributions are initially generated. Specifically, the particles at a concentration ($C$) of 0.1~1 ppm are randomly positioned in the measurement volume (size of $10 \times 10 \times 10$ mm$^3$, voxel resolution of $0.1 \times 0.1 \times 0.1$ mm$^3$). The synthetic LF images of the particles are then generated using the distortion-free LF imaging model and the particle distributions are subsequently reconstructed.

"As an example, the voxel located at (x, y, z) = (0, 0, 2) mm is considered and shows the WC estimated by DRT and BP-NN in Fig. 10. The structural similarity index matrix (SSIM) [35] is used to evaluate the similarity of WC calculated by both methods. SSIM is from 0 to 1 and a large SSIM value corresponds to a high similarity. The SSIM value of WC calculated by the DRT and BP-NN is 0.94, indicating that the estimated WC are in good agreement."
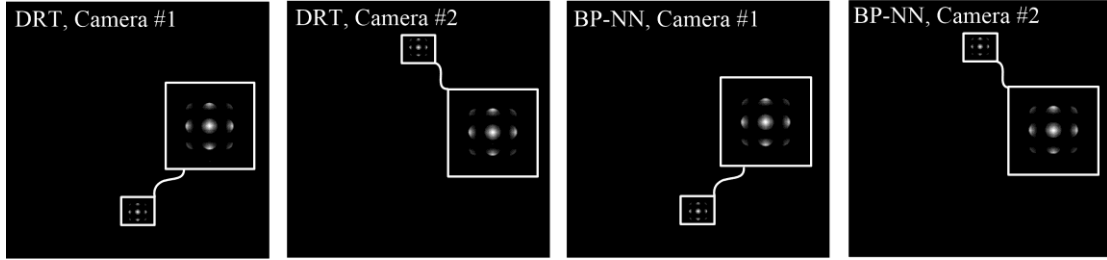


Fig. 10 Comparison of WC estimated by DRT and BP-NN methods.

Figure 11 illustrates the reconstructed particle distributions achieved by the DRT-SMART and BP-NN-SMART at $C = 0.1$ ppm. It can be seen that the particle distribution reconstructed by BP-NN-SMART [Fig. 11(c)] is similar to that of DRT-SMART [Fig. 11(b)], and both of them are in good agreement with the actual particle distribution [Fig. 11(a), ground truth]. However, some reconstructed particles are stuck together for both the BP-NN-SMART and DRT-SMART, especially in the high-density region (zoom-in figures) due to the reconstruction artefacts (e.g., ghost particles and elongation effect) arising from the limited tomographic angular views [25].

To evaluate the reconstruction quality quantitatively, two indices are defined in this study. The reconstructed accuracy ($R_{acc}$) is defined as

$$R_{acc} = \frac{\#VD}{\#VD + \#ID} \tag{13}$$

where a valid detection (VD) is defined as the presence of a single reconstructed particle within 1 voxel chessboard distance from a true particle, while an invalid detection (ID) refers to the detection of multiple particles or the absence of particle around a true particle [36], and # stands for the

number of *VD* or *ID*. The reconstructed ghosting rate ($R_g$) is defined as

$$R_g = \frac{n_{re}}{n_{tr}} \tag{14}$$

where $n_{tr}$ and $n_{re}$ denote the number of particles in the true and reconstructed particle fields, respectively. In addition to $R_{acc}$ and $R_g$, the reconstruction quality factor ($Q$) defined in [5] is also employed to assess the 3D reconstruction accuracy. The range of $R_{acc}$ and $Q$ is from 0 to 1, where a larger value indicates higher reconstruction accuracy. $R_g$ is larger than 1 and a smaller $R_g$ implies the reconstruction with fewer ghost particles.



(a) Ground truth


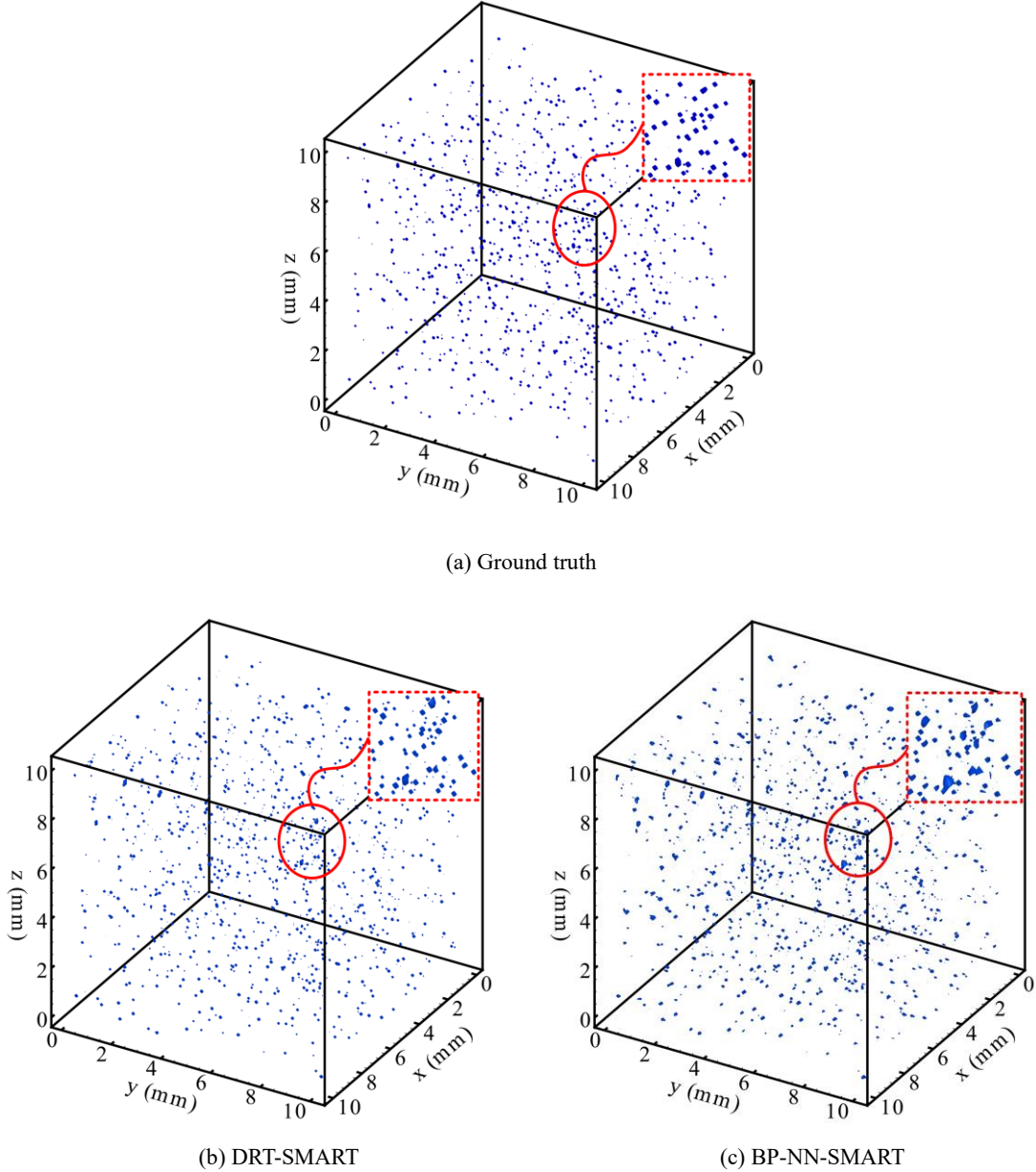
(b) DRT-SMART

(c) BP-NN-SMART

Fig. 11 3D particle distribution reconstructed by DRT-SMART and BP-NN-SMART at $C$ = 0.1 ppm.

The reconstruction accuracy, ghosting rate and quality factor of DRT-SMART and BP-NN-SMART at C = 0.1~1 ppm are depicted in Fig. 12. The range of particle concentration is chosen by considering the robustness of cross-correlation analysis, limit of the tomographic reconstruction

algorithm and the optical transmission [5, 8, 25]. From Fig. 12, it can be seen the variations of $R_{acc}$, $R_g$ and $Q$ with particle concentration are consistent for the two methods. Specifically, the number of ghost particles ($R_g$) is increased at a denser seeding concentration, resulting in a decreased reconstruction accuracy ($R_{acc}$) and reconstruction quality factor ($Q$). $R_{acc}$, $R_g$ and $Q$ of the BP-NN-SMART are similar to the DRT-SMART at different concentrations. Although the BP-NN-SMART and the DRT-SMART provide similar results in the simulation, the DRT-SMART needs prior knowledge of precise angle separation of the multi-camera system for an accurate measurement, which is difficult to obtain in practical applications. By contrast, the proposed calibration method is capable of reconstructing the particle distributions without necessitating the camera separation angles as prior knowledge.
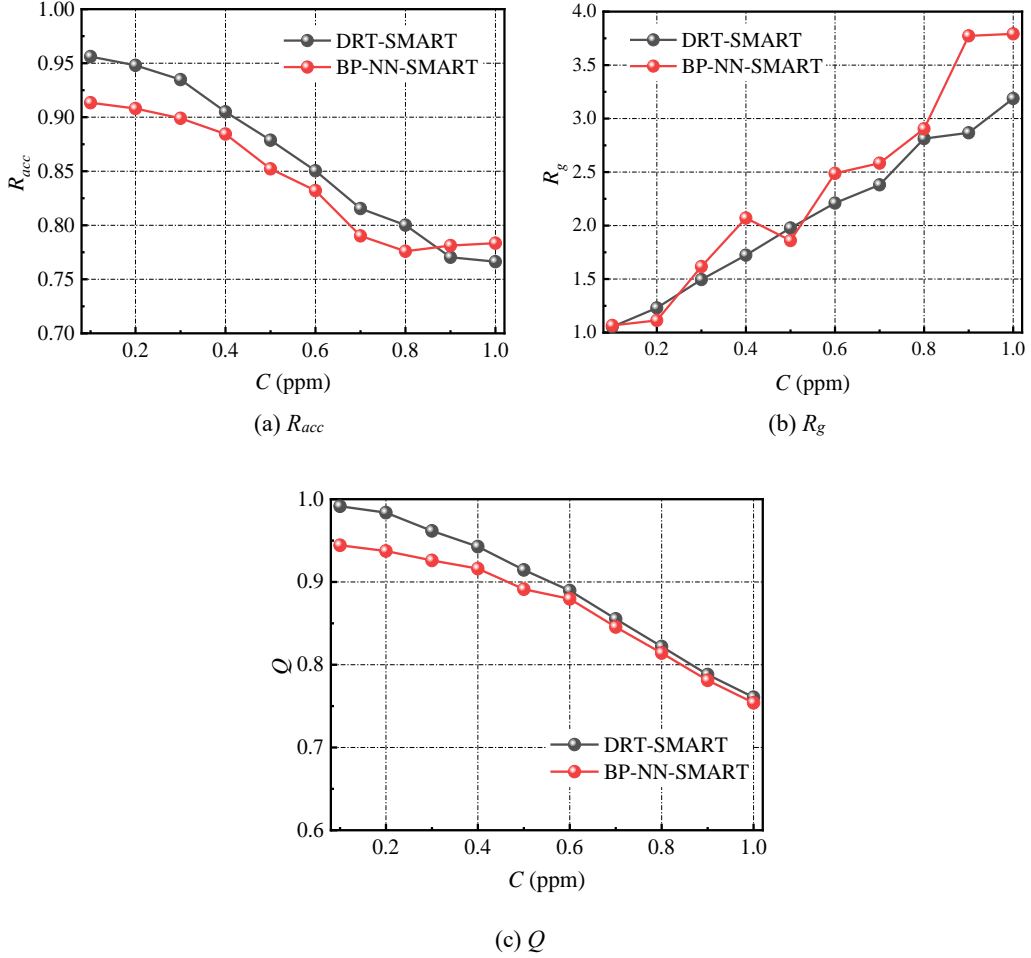


(a) $R_{acc}$

(b) $R_g$



(c) $Q$

Fig. 12 Reconstruction accuracy of DRT-SMART and BP-NN-SMART at different $C$.

## 4.2 Ring vortex field reconstruction

To achieve an accurate velocity field, the proposed calibration method is further verified through the reconstruction of a ring vortex displacement field. The analytical equation of the ring vortex can be found elsewhere in [5]. The ring vortex is located in a volume with a physical size of $14\times14\times7$ mm³ and a voxel resolution of $0.1\times0.1\times0.1$ mm³. Similar to particle distribution reconstruction, particles are randomly seeded in the measurement volume to form a 3D particle distribution. Thereafter, these particles are displaced by the ring vortex displacement field to form a new distribution. The LF images of particles are then generated and the particle volumes are

14

reconstructed by BP-NN-SMART and DRT-SMART, respectively. The CC algorithm is finally utilized to estimate the particle displacement. The displacement vectors of $35 \times 35 \times 17$ are returned in the displacement field with the interrogation volume size of $8 \times 8 \times 8$ voxels and an overlap of 50%. To evaluate the measurement accuracy of DRT-SMART and BP-NN-SMART, the CC analysis is also performed on the actual particle distributions to generate the 3D displacement field, which is taken as the ground truth as shown in Fig. 13(a).

The ring vortex fields reconstructed by the DRT-SMART and BP-NN-SAMRT at $C = 0.5$ ppm are shown in Fig. 13(b)-(d). It can be observed that the reconstruction result of BP-NN-SMART [Fig. 13(b)] is consistent with the displacement field estimated from the true particle distributions [Fig. 13(a)]. The torus-shaped vorticity field has been completely reconstructed and the magnitude of vorticity is close to the ground truth, hence demonstrating that the proposed method can facilitate an accurate 3D flow field measurement. By contrast, the accuracy of the DRT-SMART relies on the measurement accuracy of the angle separation. An accurate reconstruction can be achieved at the measured angle separation of $\Delta\alpha = 0°$. However, when the angle separation reaches $1°$, spurious vectors can be seen in the reconstruction result [marked by red circles in Fig. 13(d)].



(a) CC

(b) BP-NN-SMART

(c) DRT-SMART, $\Delta\alpha = 0°$
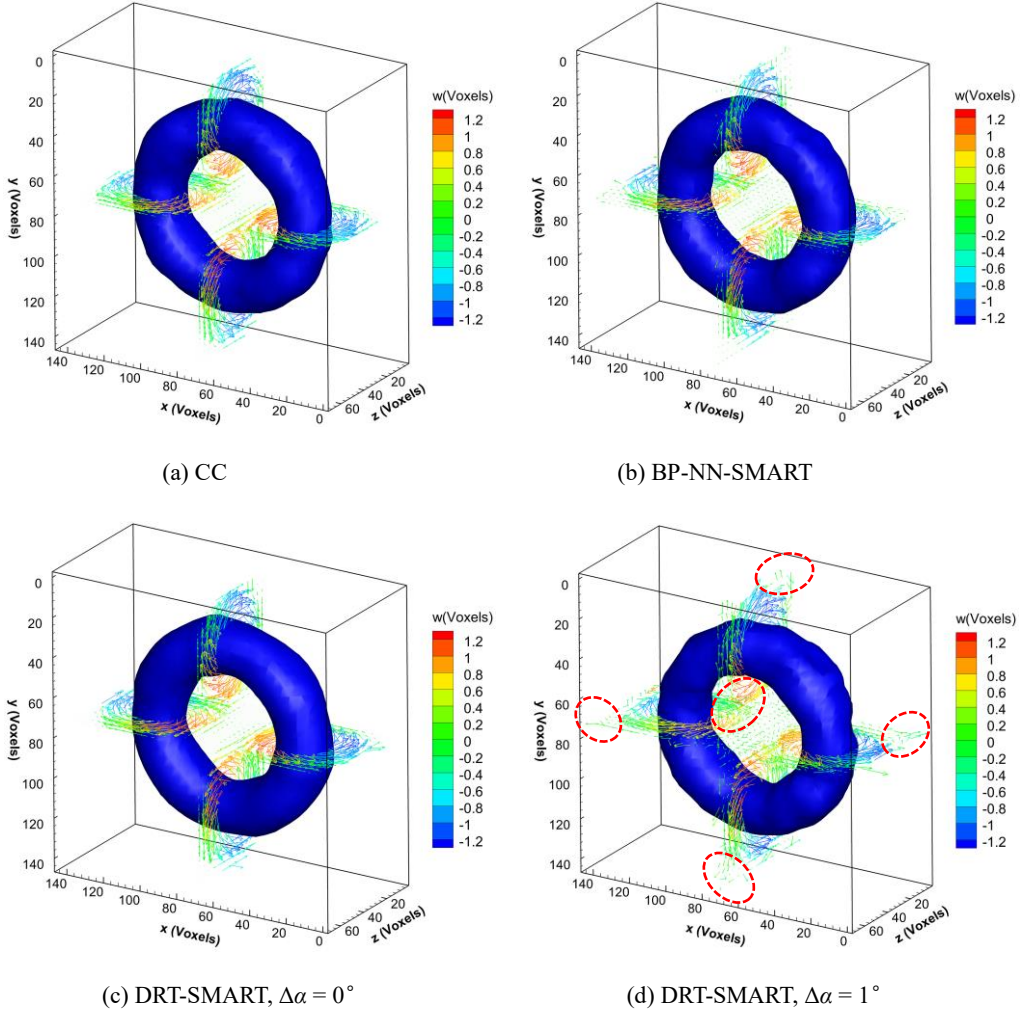
(d) DRT-SMART, $\Delta\alpha = 1°$

Fig. 13 Ring vortex field reconstructed by DRT-SAMRT and NN-SMART methods at $C = 0.5$ ppm. The iso-vorticity surface (0.12 voxels/voxel) shows the shape of the ring vortex. The vectors are colored by the magnitude of the depth velocity component ($w$).

The root mean square error (RMSE) of the reconstructed displacement vector ($\sigma_t$) is calculated by

$$\sigma_t = \sqrt{\left(u_t - u_r\right)^2 + \left(v_t - v_r\right)^2 + \left(w_t - w_r\right)^2} \tag{15}$$

where $u_t$, $v_t$, $w_t$ and $u_r$, $v_r$, $w_r$ denote the components of the true and reconstructed displacement in the $x$, $y$ and $z$-directions, respectively. For the entire displacement field containing $n_l$ vectors, the mean displacement error ($\overline{\sigma}_t$) is calculated by

$$\overline{\sigma}_t = \sum_{l=1}^{n_l} \sigma_t \Big/ n_l \tag{16}$$

Figure 14(a) depicts the $\overline{\sigma}_t$ under different particle concentrations. It shows that the $\overline{\sigma}_t$ achieved by the BP-NN-SMART is similar to the DRT-SMART at $\Delta\alpha = 0°$. However, the $\overline{\sigma}_t$ is increased significantly at $\Delta\alpha = 1°$ for the DRT-SMART. The averaged $\overline{\sigma}_t$ achieved by BP-NN-SMART at the particle concentration of 0.1 to 1 ppm is 0.35 voxels, whereas it is 0.36 and 0.71 voxels for the DRT-SMART at $\Delta\alpha = 0°$ and $\Delta\alpha = 1°$, respectively, indicating that displacement measurement error achieved by the DRT-SAMRT is closely related to the $\Delta\alpha$. This result can also be seen in Fig. 14(b), which depicts the cumulative probability function (CDF) of the $\sigma_t$ at $C = 0.5$ ppm. From Fig. 14(b), the percentage of the reconstructed displacement vectors, which has an error smaller than 0.43 voxels, is 75.6% and 64.3% for the BP-NN-SMART and DRT-SMART at $\Delta\alpha = 1°$, indicating that the BP-NN-SMART can achieve 3D flow reconstruction with higher accuracy.

For the DRT method, it is indicated that the angle separation of the LF cameras needs to be measured precisely based on the measurement volume for accurate WC estimation. Otherwise, significant errors can be involved in the 3D flow velocity measurement. This limits the use of the DRT method in practical experiments. By contrast, the proposed BP-NN method provides higher accuracy and is suitable for practical applications as it does not depend on the angle separation of LF cameras. The BP-NN method establishes the mapping relationship between the voxels and pixels based on the image features of the calibration board.
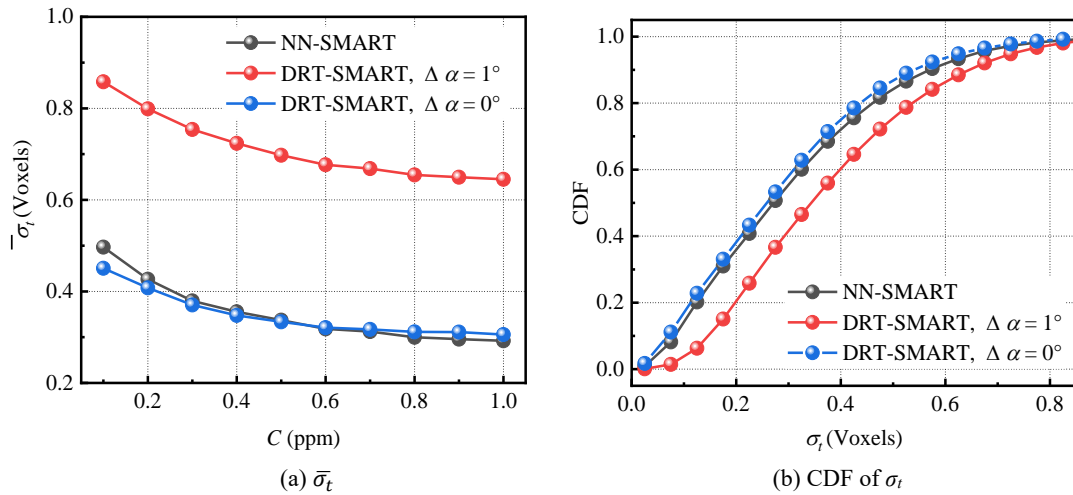


(a) $\overline{\sigma}_t$  (b) CDF of $\sigma_t$

Fig. 14 Mean displacement error ($\overline{\sigma}_t$) at $C = 0.1 \sim 1$ ppm and the cumulative probability function (CDF) of the displacement error ($\sigma_t$) at $C = 0.5$ ppm.

Table 3 shows the dataset used for training, testing and validation of the neural network. The

computational time required for calculating the WC is also added. The training of BP-NN and the WC calculation is implemented on a 44-core workstation (Intel Xeon E5-2696 v4 at 2.2GHz). A total of 197570 data is randomly split into training, validating and testing. 70% of data is used for training, 15% for validation and 15% for testing. The training process takes about 15 mins for 1000 epochs and the calculation of WC by the BP-NN model costs about 115 mins, which is very close to that achieved by the DRT method (118 mins).

Table 3: Data number and computational time in calculating the weight coefficients

| Method | BP-NN | DRT |
|---|---|---|
| Total number of data | 197570 | - |
| Training, validating and testing | 70%, 15% and 15% | - |
| Data division method | Random | - |
| Epoch number in training | 1000 | - |
| Network training time (min) | 15 | - |
| Time for calculating weight coefficients (min) | 115 | 118 |

# 5. Experimental study

## 5.1 Experimental setup

After the numerical verification, experiments were carried out on a low-swirl injector (LSI) flow to verify the BP-NN method along with the dual-camera LF-PIV system. The schematic and photograph of the LSI are shown in Fig. 15. The LSI configuration encompasses an annual swirler consisting of the curved vanes and the center-body. The inner radius of the center-body ($R_c$) is 12 mm and a perforated screen with 30 round holes (diameter of 2 mm) is fitted at its entrance. The presence of a perforated screen enables a fraction of the air to bypass the swirler, thereby forming a swirl flow with a small recirculation zone downstream of the injector [37]. Eight curved vanes with a length ($L_p$) of 22 mm and angle ($\theta_s$) of 37° are connected with the central channel screen. The swirl number ($S$) for LSI can be calculated by [38]

$$S = \frac{2}{3}\tan\alpha \frac{1-r^3}{1-r^2 + m^2 r^2((1/r^2)-1)^2} \tag{17}$$

where $m$ denotes the ratio between the mass flow from the central channel and the swirled annulus, and $r$ denotes the ratio of the central channel radius to the injector radius. According to Eq. (17), the swirl number of the current swirl injector is 0.55.



Low swirl injector      8 swirl blades      Center channel screen
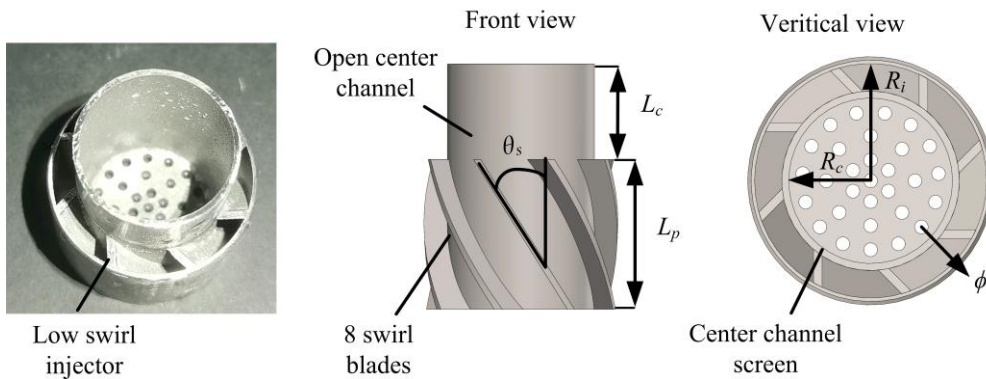
Fig. 15 Schematic and photograph of the low-swirl injector.

Figure 16 illustrates the experimental setup of the LSI flow. The supplied air seeded with the tracer particles passes through the injector to form the 3D swirl flow. The airflow is regulated using a mass flow controller with a precision of 1% to maintain a constant flow rate of 200 L/min. The bulk velocity based on the diameter of the injector ($D = 34$ mm) is 3.67 m/s. The tracers used in this experiment are titanium dioxide particles (Beiting Measurement Technologies, China) with a melting point of 1840 centigrade. The density of the particle is 4.2 g/cm$^3$ and the mean particle size is 5 µm. Low agglomeration of particles occurs due to the hydrophobic surface of the particles. The Stokes number of the tracer particles is estimated as 0.026. A value of the Stokes number below 0.1 can yield an acceptable accuracy for flow tracing [39]. To measure the 3D swirl flow, a dual-pulse laser (energy of 200 mJ/pulse, repetition frequency of 15 Hz) coupled with a beam expander and slits is used to provide illumination for the test flow field. Two LF cameras with a separation angle of about 40° are employed to capture the LF images of the tracer particles from different perspectives. The optical settings of the LF cameras are listed in Table 2.
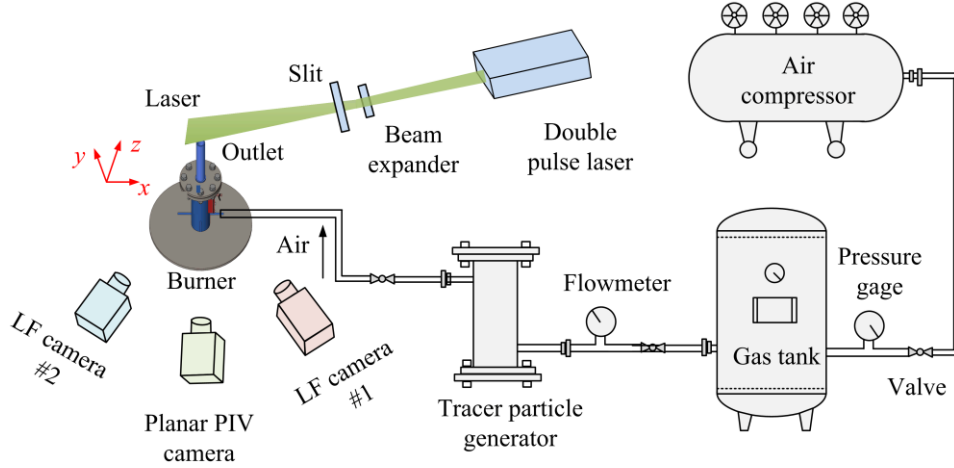


Fig. 16 Schematic of the experimental setup of the LSI flow measurement.

Figure 17 illustrates the defined world coordinate and the position of the field of view of the dual-camera LF-PIV system. The origin is located at the center of the injector outlet plane. The $y$-axis corresponds to the axial directions of the flow and the $z$-axis is aligned between two LF cameras. The bottom of each camera's field of view is roughly $0.35D$ downstream of the injector outlet. The reconstructed volume spans $13 \times 10 \times 12$ mm$^3$ ($0.37D \times 0.29D \times 0.35D$) in physical size and it is discretized into $130 \times 100 \times 120$ voxels. The SMART is utilized to reconstruct the 3D particle distributions in the measurement volume (10 iterations, $\mu = 1.0$). Using the $16 \times 16 \times 16$ interrogation window with 50% overlap, $16 \times 12 \times 15$ velocity vectors are obtained from the CC analysis. A total of 150 image pairs are reconstructed to particle volumes and the corresponding instantaneous velocity fields are acquired for statistical evaluation.

The calibration procedure of the dual-camera LF-PIV system is conducted using the same optical settings as in experiments. Specifically, a calibration board composed of a $7 \times 7$ dot point array (grid spacing of 0.5 mm, dot diameter of 0.1 mm) is placed above the outlet of the injector. The calibration board is moved along the depth direction in the range of -6 mm $< z <$ 6 mm with a uniform interval of 1 mm. The LF images of the calibration board are recorded for dual-camera
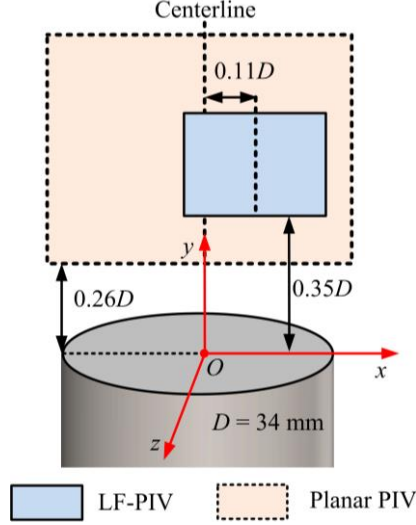
calibration by the BP-NN method.



Fig. 17 Field of view of the LF-PIV cameras and planar PIV camera in the LSI flow measurement.

To assess the measurement accuracy of the proposed system, planar PIV measurements are conducted in a similar configuration. The optical settings of the planar PIV and the camera are summarized in Table 2. The field of view (FOV) of the camera is $40 \times 30$ mm$^2$ ($1.18D \times 0.88D$). The FOV is always perpendicular to the outlet plane of the LSI, thus only the in-plane component of the test flow can be measured. The camera is moved by a linear translation stage to focus on three different depth planes ($z$ = -0.45$D$, -0.30$D$, -0.15$D$), and their measured velocities are compared with that of the LF-PIV. In the cross-correlation analysis of planar-PIV, a final interrogation window of $32 \times 32$ voxels with 50% overlap is utilized, generating a 2D velocity field with $171 \times 131$ vectors. The velocity vector has a spatial resolution of $0.43 \times 0.43$ mm$^2$. A total of 600 image pairs are recorded at each depth plane and processed to obtain the time-averaged velocity field.

## 5.2 Reconstruction of a calibration board

Through the calibration of the dual-camera LF-PIV system, the dot centers on the calibration board are reconstructed and depicted in Fig. 18. The contour on the right side shows the depth of the reconstructed dots. It can be seen that the $7 \times 7$ dot arrays with uniform grid spacing and depth separations have been completely reconstructed. Due to that the actual grid spacing of the dot array and the translation distance of the calibration board are known. Thus, the mean lateral and depth reconstruction error of the dot center ($\sigma_l$ and $\sigma_d$) can be calculated as

$$\sigma_l = \sum_{i}^{n_d} \left| l_{r,i} - l_t \right| \bigg/ n_d \tag{18}$$

$$\sigma_d = \sum_{i}^{n_d} \left| d_{r,i} - d_t \right| \bigg/ n_d \tag{19}$$

where $l_{r,i}$ is the lateral spacing between the $i_{th}$ dot and its adjacent dot (shown in the enlarged figure in Fig. 18), $l_t$ is the true grid spacing (1 mm), $d_{r,i}$ is the depth separation of the dots on adjacent arrays, $d_t$ is the true depth interval (1 mm) and $n_d$ is the number of dots.
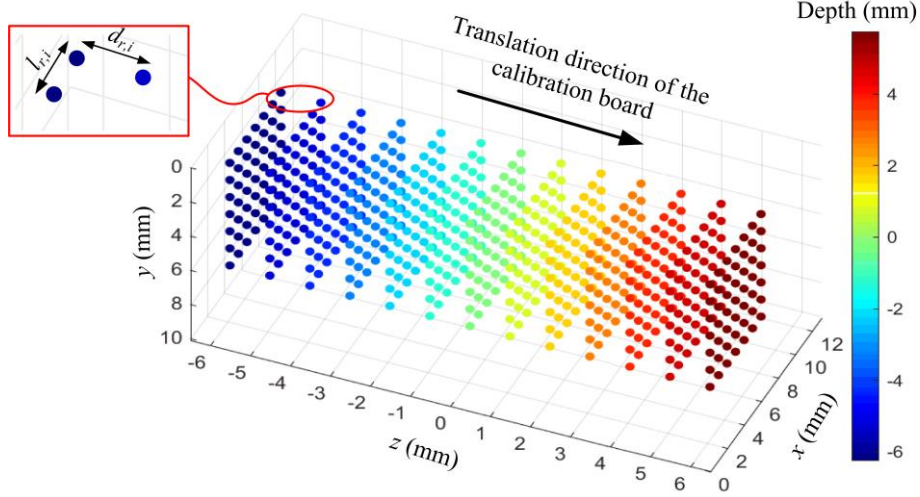
Fig. 18 Reconstructed dot point centers on the calibration board located at -6 mm < $z$ < 6 mm.

Figure 19 illustrates the variations of the $\sigma_l$ and $\sigma_d$ with the depths. In the depth range of -6 mm < $z$ < 6mm, the mean lateral reconstruction error is 0.08 mm, which is smaller than the microlens pitch (0.1 mm). The depth reconstruction error is slightly larger than the lateral error and the averaged value is 0.25 mm. This result indicates that the dual-camera system incorporating the BP-NN calibration procedure can reconstruct the 3D locations of the feature dots accurately.
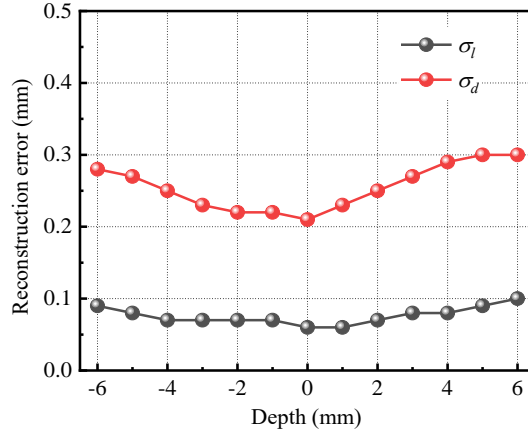


Fig. 19 Variation of lateral and depth reconstruction errors of the feature dot on the calibration board.

## 5.3 Reconstruction of a LSI flow field

The calibration result of the dual-camera LF-PIV system is further used to reconstruct the 3D LSI flow. Figure 20 illustrates the time-averaged velocity fields measured by the planar PIV at $z$ = -0.45$D$, -0.3$D$, -0.15$D$. The same depth planes are also extracted from the 3D dual-camera LF-PIV data for comparison (Fig. 21). From Figs. 20 and 21, it can be observed that as the depth plane approaches the injector center ($z/D$ = 0), the maximum axial velocity gradually decreases, and the radial position where the maximum axial velocity moves towards the edge. At the depth plane of $z$ = -0.15$D$, low velocity is demonstrated at the central region ($x/D$ = 0). The velocity magnitude in this region is close to zero and strong recirculation is not observed. This has been investigated by Johnson et al. [38] for a LSI with an estimated swirl number of $S$ = 0.5. Furthermore, in the depth

range of *z/D* < 0, the direction of the radial velocity component is consistently leftward at different depths, which is in line with the direction of the swirler vanes (shown in Fig. 15). The magnitude of the radial velocity decelerates with decreasing the depth distance to the central depth of the injector. The result in Figs. 20 and 21 also demonstrate a satisfactory agreement between the measurement results of the dual-camera LF-PIV and planar PIV at different depths.



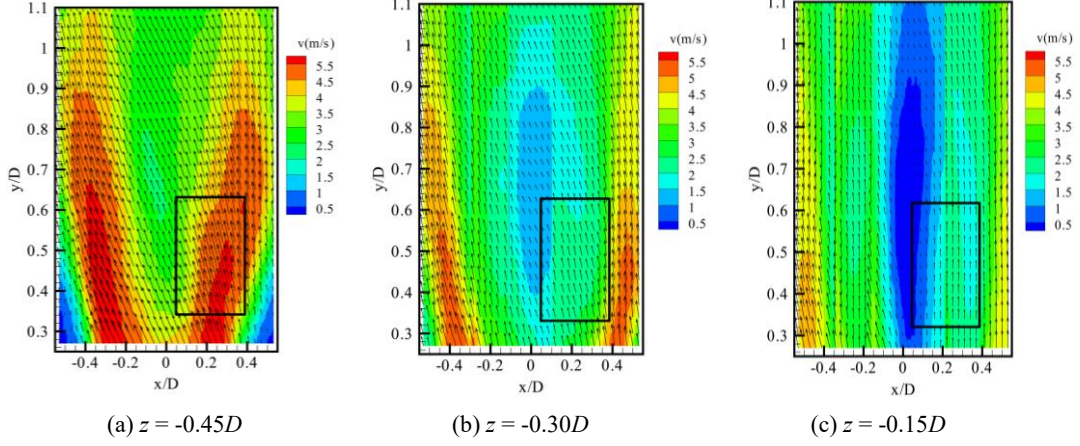(a) *z* = -0.45*D*    (b) *z* = -0.30*D*    (c) *z* = -0.15*D*

Fig. 20 LSI velocity field distribution at different depth planes measured by planar PIV. The black boxes show the field of view of the dual-camera LF-PIV.



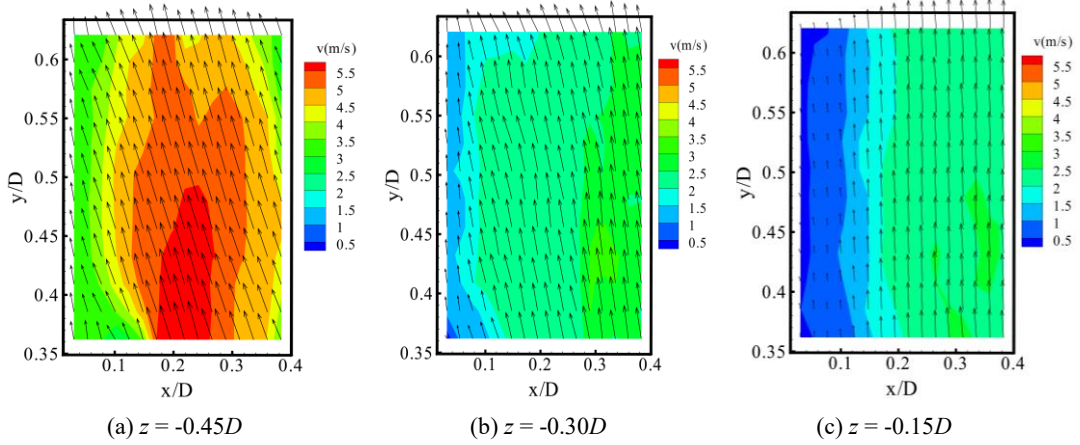(a) *z* = -0.45*D*    (b) *z* = -0.30*D*    (c) *z* = -0.15*D*

Fig. 21 LSI velocity field at different depths extracted from 3D data of the dual-camera LF-PIV.

To assess the measurement accuracy of the dual-camera LF-PIV quantitatively, the time-averaged velocity distribution along the axial direction (*y*) at *x/D* = 0.2 is extracted and depicted in Fig. 22. The *u* and *v* in this figure are the radial and axial velocity components, respectively. It can be observed that the *u* and *v* achieved by the dual-camera LF-PIV are slightly larger than the planar PIV at different depths. Compared with the planar PIV, the mean error of *u* and *v* components achieved by the dual-camera LF-PIV are 9.05% and 9.89%, respectively. This further validates that the dual-camera LF-PIV system in combination with the BP-NN calibration method can achieve accurate 3D flow measurement.
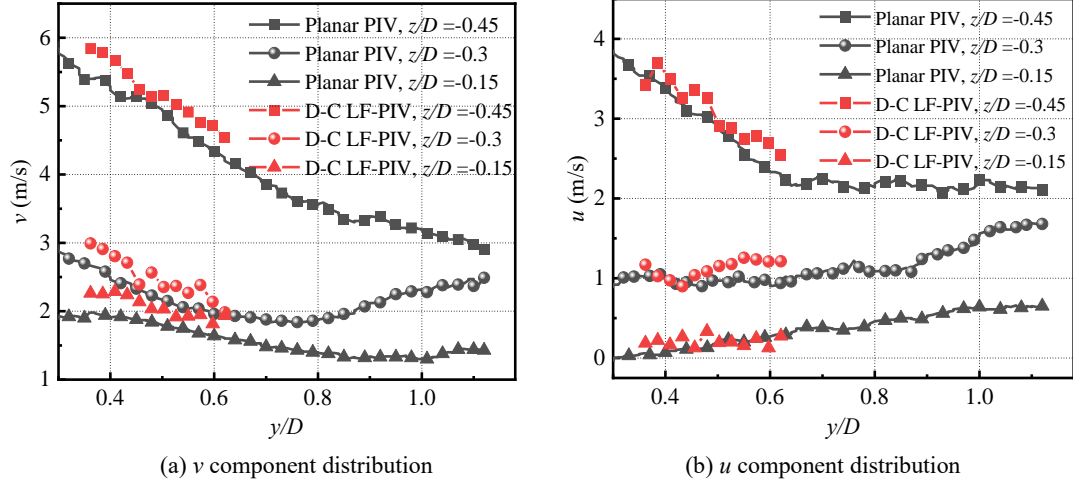
(a) *v* component distribution       (b) *u* component distribution

Fig. 22 Time-averaged velocity distribution along the axial direction (*y*-axis) at $x/D = 0.2$, $z/D = -0.45$, -0.3 and -0.15 measured by planar PIV and dual-camera (D-C) LF-PIV.

## 6. Conclusion

This study proposes a backpropagation neural network (BP-NN) based calibration method of multi-camera LF-PIV for an accurate weight coefficient (WC) estimation and particle distribution reconstruction. A comparative study is conducted through synthetic tests of particle distribution reconstruction and ring vortex field reconstruction with the conventional direct ray tracing method (DRT). Experiments on a low-swirl injector (LSI) flow are further carried out to verify the performance of the BP-NN method. The concluding remarks are summarized as follows:

- For the WC estimation, the error of angle separation between the LF cameras and the measurement volume must be corrected for the DRT method, otherwise, significant errors are involved in the 3D flow field measurement. Synthetic tests show that an error of angle separation of 1° leads to twice the root mean square error of the ring vortex displacement field.

- The proposed BP-NN calibration method compensates for the optical distortions of the imaging system and does not depend on the angle separation of the multiple cameras as prior knowledge. Therefore, it is easy to implement in practical experiments and provides higher accuracy in the WC estimation.

- A dual-camera LF-PIV system incorporating the proposed calibration method can achieve accurate particle reconstruction and 3D flow measurement. At the particle concentration of 0.1 to 1 ppm, the particle reconstruction quality factor of 0.75 can be achieved. The relative errors of axial and radial velocity components of the LSI flow are 9.05% and 9.89%, respectively.

In future, the multiple-camera LF-PIV incorporating the proposed calibration method will be applied to different 3D flow patterns for investigating more complex flow structures. Furthermore, efforts will be also made to increase the measurement domain of the LF-PIV by enlarging the field of view of the LF cameras.

## Declaration of Competing Interest

The authors declare that they have no known competing financial interests or personal

relationships that could have appeared to influence the work reported in this paper.

# References

[1] Kankanwadi K S, Buxton O R H. On the physical nature of the turbulent/turbulent interface[J]. Journal of Fluid Mechanics, 2022, 942: A31.

[2] Westerweel J, Elsinga G E, Adrian R J. Particle image velocimetry for complex and turbulent flows[J]. Annual Review of Fluid Mechanics, 2013, 45, 409-436.

[3] Fahringer T W, Lynch K P, Thurow B S. Volumetric particle image velocimetry with a single plenoptic camera[J]. Measurement Science and Technology, 2015, 26: 115201.

[4] Shi S, Ding J, Atkinson C, et al. A detailed comparison of single-camera light-field PIV and tomographic PIV[J]. Experiments in Fluids, 2018, 59: 1-13.

[5] Reference details omitted for double-anonymized reviewing.

[6] Deem E A, Zhang Y, Cattafesta L N, et al. On the resolution of plenoptic PIV[J]. Measurement Science and Technology, 2016, 27: 084003.

[7] Gu M, Xu C, Hossain M M, et al. A low-rank decomposition-based deconvolution algorithm for rapid volumetric reconstruction of light field μPIV[J]. Experiments in Fluids, 2023, 64(2): 1-15.

[8] Fahringer T W, Thurow B S. Plenoptic particle image velocimetry with multiple plenoptic cameras[J]. Measurement Science and Technology, 2018, 29: 075202.

[9] Reference details omitted for double-anonymized reviewing.

[10] Mei D, Ding J, Shi S, et al. High-resolution volumetric dual-camera light-field PIV[J]. Experiments in Fluids, 2019, 60: 132.

[11] Song X, Gu M, Cao L, et al. A micro particle image velocimetry based on light field imaging. IEEE Sensors Journal, 2019, 19(21): 9806-9817.

[12] Tan Z P, Johnson K, Clifford C, et al. Development of a modular, high-speed plenoptic-camera for 3D flow-measurement[J]. Optics Express, 2018, 27(9): 13400-13415.

[13] Reference details omitted for double-anonymized reviewing.

[14] Shi S, Ding J, New TH, et al. Light-field camera-based 3D volumetric particle image velocimetry with dense ray tracing reconstruction technique[J]. Experiments in Fluids, 2017, 58: 78.

[15] Wieneke B. Improvements for volume self-calibration[J]. Measurement Science and Technology, 2018, 29(8): 084002.

[16] Soloff S M, Adrian R J, Liu Z. Distortion compensation for generalized stereoscopic particle image velocimetry[J]. Measurement Science and Technology, 1997, 8(12): 1441-1454.

[17] Bok Y, Jeon H, Kweon I. Geometric calibration of micro-lens-based light field cameras using line features[J]. IEEE Transactions on Pattern Analysis and Machine Intelligence, 2017, 39(2): 287-300.

[18] Sun J, Hossain M M, Xu C, et al. A novel calibration method of focused light field camera for 3D reconstruction of flame temperature[J]. Optics Communications, 2017, 390(5): 7-15.

[19] Shi S, Ding J, New T H, et al. Volumetric calibration enhancements for single-camera light field PIV[J]. Experiments in Fluids, 2019, 60(1): 21.

[20] Hall E M, Fahringer T W, Gulidenbecher D R, et al. Volumetric calibration of a plenoptic camera[J]. Applied Optics, 2018, 57(4): 914-923.

[21] Zhao Z, Ding J, Shi S, et al. Volumetric flow characterization of a rectangular orifice impinging synthetic jet with single-camera light-field PIV[J]. Experimental Thermal and Fluid Science, 2021, 123(5): 110327.

[22] Jones C, Bolton Johnathan, Clifford C, et al. Single-camera three-dimensional velocity measurement of a fin-

generated shock-wave/boundar-layer interaction[J]. AIAA Journal, 2020, 58(10): 4438-4450.

[23] Zhao Z, Shi S. Volumetric calibration for scheimpflug light field PIV[J]. Experiments in Fluids, 2021, 62(11): 251.

[24] Wieneke B. Volume self-calibration for 3D particle image velocimetry[J]. Experiments in Fluids, 2008, 45(6): 549–556.

[25] Scarano F. Tomographic PIV: principles and practice[J]. Measurement Science and Technology, 2013, 24(10): 012001.

[26] Ng R. Digital light field photography[D]. Stanford University, 2006: 11-19.

[27] Salvi J, Armangué X, Batle J. A comparative review of camera calibration methods with accuracy evaluation[J]. Pattern Recognition, 2002, 35(7): 1617-1635.

[28] Fei R, Merzkirch W. Investigations of the measurement accuracy of stereo particle image velocimetry[J]. Experiments in Fluids, 2004, 37(6): 559-565.

[29] Dou J, Pan C, Liu J. Robustness of neural network calibration model for accurate spatial positioning[J]. Optics Express, 2021, 29(21): 32922-32938.

[30] Deo I K, Jaiman R. Predicting waves in fluids with deep neural network[J]. Physics of Fluids, 2022, 34(6): 067108.

[31] Chang J, Chen Y. Pyramid stereo matching network[C]. Proceedings of the IEEE Conference on Computer Vision and Pattern Recognition, 2018, 5410-5418.

[32] Gim Y, Jang D K, Sohn D K, et al. Three-dimensional particle tracking velocimetry using shallow neural network for real-time analysis[J]. Experiments in Fluids, 61(1): 26.

[33] Atkinson C, Soria J. An efficient simultaneous reconstruction technique for tomographic particle image velocimetry[J]. Experiments in Fluids, 2009, 47(8): 553-568.

[34] Fahringer T W, Thurow B S. Filtered refocusing: a volumetric reconstruction algorithm for plenoptic-PIV[J]. Measurement Science and Technology, 2016, 27(9): 094005.

[35] Z. Wang, A.C. Bovik, H.R. Sheikh, E.P. Simoncelli, Image quality assessment: From error visibility to structural similarity, IEEE Trans. Image Process. 13 (2004) 600–612.

[36] Cornic P, Leclaire B, Champagnat F, et al. Double-frame tomographic PTV at high seeding densities[J]. Experiments in Fluids, 61 (1): 23.

[37] Peterson P, Olofsson J, Brackman C, et al. Simultaneous PIV/OH-PLIF, Rayleigh thermometry/OH-PLIF and stereo PIV measurements in a low-swirl flame[J]. Applied Optics, 2007, 46(19), 3298-3936.

[38] Johnson M R, Littlejohn D, Nazeer W A, et al. A comparison of the flow fields and emissions of high-swirl injectors and low-swirl injectors for lean premixed gas turbines[J]. Proceedings of the Combustion Institute, 2005, 30(2): 2867-2874.

[39] Samimy M, Lele S K. Motion of particles with inertia in a compressible free shear layer[J]. Physics of Fluids, 1991, 3: 1915-1923.